Supporting Information for

Ultrasensitive, Mechanically Responsive Optical Metasurfaces *via* Strain Amplification

Wenxiang Chen[a], Wenjing Liu[b], Yijie Jiang[c], Mingliang Zhang[a.b.d], Naixin Song[b], Nicholas J. Greybush[b], Jiacen Guo[b], Anna K. Estep[c], Kevin T. Turner[c,b], Ritesh Agarwal[b], Cherie R. Kagan[a,b,d,*]

[a]Department of Electrical and Systems Engineering, [b]Department of Materials Science and Engineering, [c]Department of Mechanical Engineering and Applied Mechanics, [d]Department of Chemistry, University of Pennsylvania, Philadelphia, PA 19104, USA

[*]*To whom correspondence should be addressed.*

Cherie Kagan

Address: 200 South 33rd Street, 364 Levine Hall, Philadelphia, PA 19104.

E-mail: kagan@seas.upenn.edu

Phone : (215) 573-4384. Fax : (215) 573-2068

Design of tapered microrods: The design of the microrods was developed by considering their influence on the distribution of local strain (ε_{loc}) and the deformation of the Au nanolines upon the application of external strain (ε_{ex}).

For the non-tapered microrod design, ε_{loc} is highly concentrated at single spots near the corners of the microrods, as shown by the finite element (FE) modeling result in Figure S1c. ε_{loc} near the corners of the microrods is about 58% upon the application of ε_{ex} = 3%. ε_{loc} along the topline of the microrod is about 35% on average. For the tapered microrods, the local maximum strain is distributed along the topline of the trapezoids, which is approximately 53% (Figure S3a). The tapered microrod design focuses strain within the gap between the pair of microrods where the grating is positioned, while the non-tapered microrod design results in high strain at the corners of the microrods, which are away from the grating. The tapered microrod design was chosen as it provides an effective concentration of strain on the grating.

Related to the strain concentration at the corners, we also find that the non-tapered microrod design leads to a more non-uniform strain distribution along the x-direction and thus larger bending in the Au nanolines in the grating. The displacement (u_y) of the 1st, 6th, 12th Au nanolines in the grating (counting from top to bottom) at ε_{ex} = 3% are plotted for the tapered microrod with 10 μm topline (A = 10 μm, Figure S1d), the tapered microrod with 13 μm topline (A = 13 μm, Figure S1e), and the non-tapered microrod (A = 20 μm, Figure S1f), respectively (design parameters in Figure 1b). For the tapered microrod with 10 μm topline, the 1st Au nanoline is bent both concavely and convexly and therefore the deformation in Au nanoline is neutralized to certain degree. For the tapered microrod with 13 μm topline and the non-tapered

microrod, the Au nanolines are bent mostly concavely. The average displacement ($\overline{u\_y}$) of each Au nanoline is indicated in the figure S1d-f. Comparatively, the tapered microrod with 10 μm topline creates the smallest standard errors in $\overline{u\_y}$ of the Au nanolines. We choose the tapered microrods with 10 μm topline to also reduce the variation in u_y and therefore the deformation in Au nanolines.

The displacement of the experimentally fabricated Au nanolines at ε_{ex} = 11.8% is analyzed for the tapered microrods with L = 40 μm, G = 16 μm (Figure 3c, Figure S1g) and L = 120 μm, G = 16 μm (Figure 3g, Figure S1h). The Au nanolines remain flat for the microrods of L = 40 μm, G = 16 μm (Figure S1g). The microrod with L = 120 μm creates higher ε_{loc} in the grating, which bends the Au nanolines to a small degree. The bending of the Au nanolines and the non-uniformity in ε_{loc} in the y-direction could likely be further reduced with more advanced metastructure geometries, but extensive optimization studies would be required to develop such designs.

Cyclical stretching of the plasmonic grating on microstructured elastomeric substrate: The metastructure with L = 120 μm and G = 16 μm is cyclically stretched 10 times between $\varepsilon_{ex} = 0\%$ and 9.1%. There is a deviation (± 19 nm) in p' at ε_{ex} = 9.1%. We find that the deviation is consistent with a slight buckling of the microrods in the cycling processes (shown in Figure S15). The roughness of the Au layer on PDMS substrate and the buckling of the Au layer upon application of external strain have also been reported in previous publications.[1–3]

Discussion on the limit of the mechano-sensitivity: To discuss the limit of the mechano-sensitivity of the metastructure, we need to consider the magnitude of the applied ε_{ex} at the same time. At the same magnitude of the applied ε_{ex}, higher $A_{sensitivity}$ can result in higher ε_{loc} around the metastructure on the PDMS substrate, which can eventually lead to plastic deformation of the metastructure/PDMS and/or delamination at the Au-PDMS interface. To give an example, for ε_{ex} = 9.1%, we demonstrate in experiments and simulations that $A_{sensitivity}$ can be tuned from 0.9 to 8.8 by increasing the length of the microrods (L) or decreasing the gap between the microrods (G). In Table 2 we show that $\varepsilon_{spacing}$ in the grating increases from 18% to 188% as $A_{sensitivity}$ increases. It is possible to further improve $A_{sensitivity}$ by further increasing L or decreasing G. However, at the same time, the ε_{loc} around the metastructure will also increase, and eventually cause plastic deformation in the metastructure/PDMS or delamination at the Au-PDMS interface. The limit of the mechano-sensitivity is reached when the plastic deformation in the device occurs or the metastructure delaminates from the substrate. It should be noted that for a smaller ε_{ex}, for example 3%, the limit of $A_{sensitivity}$ will be larger than that for ε_{ex} = 11.8%, since the smaller ε_{ex} will create a smaller ε_{loc} around the metastructure on the PDMS substrate.

To improve the limit of $A_{sensitivity}$, the maximum strain that the metastructure/PDMS and the interface can withstand needs to be enhanced. Some possible ways are to fabricate microrods from other materials that have higher yield strain than Au (for example, Ni), use emerging elastomeric substrates that have higher yield strain than PDMS, and optimizing the bonding at the interface between the metasurface and the elastomer substrate.

Surface lattice resonances based on plasmonic gratings: Surface lattice resonances arise from the hybridization of the diffractive orders propagating parallel to the substrate surface and the transverse LSPR from the individual Au nanolines in the plasmonic grating. The wavelength of the surface lattice resonance is determined by both p and the incident angle, as shown in eqs 2 and 3 in main text. As an example, the surface lattice resonances originating from the hybridization of the first-order substrate mode of λ_D and the transverse LSPR from the individual Au nanolines at normal incidence is calculated by FDTD simulation and plotted as a function of p in Figure 5c in main text. As p increases from 470 nm to 670 nm and therefore λ_D gradually moves away from the hybridization regime (Figure 5b in main text), the full width at half maximum (fwhm) of the resonance remains narrow at 72 ± 31 nm due to diffraction. The resonance amplitude decreases from 85% to 30% because of progressively weaker coupling between the diffraction mode and the transverse LSPR of the individual Au nanolines.

Scattering efficiency of the plasmonic grating: We investigate the scattering of the plasmonic grating. The scattered light from the plasmonic grating is dominated by the diffractive orders. We calculated the 0^{th} order and 1^{st} order of diffraction (m = 0, ±1) from the grating (w = 200 nm, p = 500 nm, t = 80 nm) by FDTD simulation to illustrate the scattering efficiency (schematic in Figure S16a). Diffractive orders higher than 1 are not considered here as they are not supported by the grating in the wavelength range we investigate. We calculate the relative ratio of the intensity of the 0^{th} order and 1^{st} order diffraction, with the incident angle (θ) varying between 0° and 45° and the incident wavelength varying between 400 nm and 1500 nm. The scattering efficiency of the grating (or the percentage of the 1^{st} order diffraction in the diffracted light) depends on both θ and the incident wavelength, as shown in Figure S16d,g,j,m. As θ increases, a

wider range of wavelengths is scattered in the 1st order diffraction. Most light is scattered at θ = 45°, where the scattered light wavelength ranges from 400 nm to 850 nm and the angle (θ') varies between -9° and -90° (Figure S16l). The scattering efficiency (shown as relative ratio) approximately varies between 0 and 0.7 (Figure S16m) at different wavelengths.

Angle-resolved reflectance spectra: In the angle-resolved reflectance spectra, there is a standard deviation in the amplitude of the resonances (± 7.2%). The standard deviation may arise from the slight variation in the light source profile over the measurement time. Another possibility is that there is a standard deviation in the spot size of the focused incident light on the plasmonic grating during the measurements at various ε_{ex}. Variation in spot size could result in a difference in reflectance in the angle-resolved reflectance spectra.

There is a discrepancy in the linewidth of the resonance and the resonance wavelength between the experiment and simulation results, which we hypothesize is due to fabrication tolerances in the dimensions of fabricated metastructures.[4] For example, in experiment, the fabrication results yield w = 206 ± 11 nm and p = 454 ± 16 nm (ε_{ex} = 0%). In simulation, these variations are not captured. Another possible reason for the discrepancy in the resonance wavelength is that the Au nanolines could partly sit inside the PDMS substrate after the fabrication, while in FDTD simulation we assume the Au nanolines sit on the surface of the PDMS substrate.

Linear fits of the reflectance peak positions as a function of ε_{ex}: In the angle-resolved reflectance measurements, we obtain the wavelength of the surface lattice resonances at normal incidence (Figure 6n in main text) at various ε_{ex}. Linear fitting is used to fit the experimental $\text{resonance} = 47.7 \times \varepsilon_{ex} \times 100 + 675.6$ (black dashes) and simulated $\text{resonance} = 38.9 \times \varepsilon_{ex} \times 100 + 678.1$ (red dashes) with r-square at or above 0.96.

References

(1) Zhang, J.; Yan, Y.; Miao, P.; Cai, J. Fabrication of Gold-Coated PDMS Surfaces with Arrayed Triangular Micro/nanopyramids for Use as SERS Substrates. *Beilstein J. Nanotechnol.* **2017**, *8*, 2271–2282.

(2) Lacour, S. P.; Jones, J.; Wagner, S.; Li, T.; Suo, Z.. Stretchable Interconnects for Elastic Electronic Surfaces. *Proc. IEEE* **2005**, *93*, 1459–1467.

(3) Rogel, R.; Borgne, B. L.; Mohammed-Brahim, T.; Jacques, E.; Harnois, M. Spontaneous Buckling of Multiaxially Flexible and Stretchable Interconnects Using PDMS/Fibrous Composite Substrates. *Adv. Mater. Interfaces* **2017**, *4*, 1600946.

(4) Caglayan, H.; Hong, S.-H.; Edwards, B.; Kagan, C. R.; Engheta, N. Near-Infrared Metatronic Nanocircuits by Design. *Phys. Rev. Lett.* **2013**, *111*, 073904.

Table S1 A comparison of the mechano-sensitivities of the optical responses of different stretchable metasurfaces in recent publications.

Mechano-sensitivity (nm/1% ε_{ex} variation)	Structure	Wavelength	Elastic (Y/N)	Maximum ε_{ex} applied	Reference (in main text)
3	Au asymmetric coupled split ring resonator	Mid-IR	N	50%	22
5	Au nanodisk array	Visible to near IR	Y	107%	23
14	Au pyramid array	Visible	Unknown	9%	24
4	Al nanoparticle array	Visible	Y	50%	26
5	TiO_2 nanoparticle array	Visible	Unknown	6%	28
2	Au nanoribbon array	Visible to near IR	Unknown	14%	29
5	Al nanoparticle array	Visible	Y	32%	30
48	Au grating	Near IR	Y	12%	Our work

Table S2. A summary of mechanical parameters used to characterize A_{strain} and $A_{sensitivity}$ for metastructures with different G and L.

G (μm)	L (μm)	$p \pm \Delta p$ (nm)	$p' \pm \Delta p$ (nm)	$\varepsilon_{spacing}$ (%)	I_{pitch} (%)	A_{strain}	$A_{sensitivity}$
+∞	0	513 ± 22	569 ± 20	18.1	10.9	1.5	0.9
120	80	512 ± 20	579 ± 16	21.7	13.1	1.9	1.1
60	80	512 ± 13	586 ± 15	23.9	14.5	2.0	1.2
16	80	474 ± 17	799 ± 46	119.9	68.6	10.2	5.8
16	40	499 ± 16	684 ± 21	62.5	37.1	5.3	3.1
16	120	454 ± 16	926 ± 52	188.0	104.0	15.9	8.8

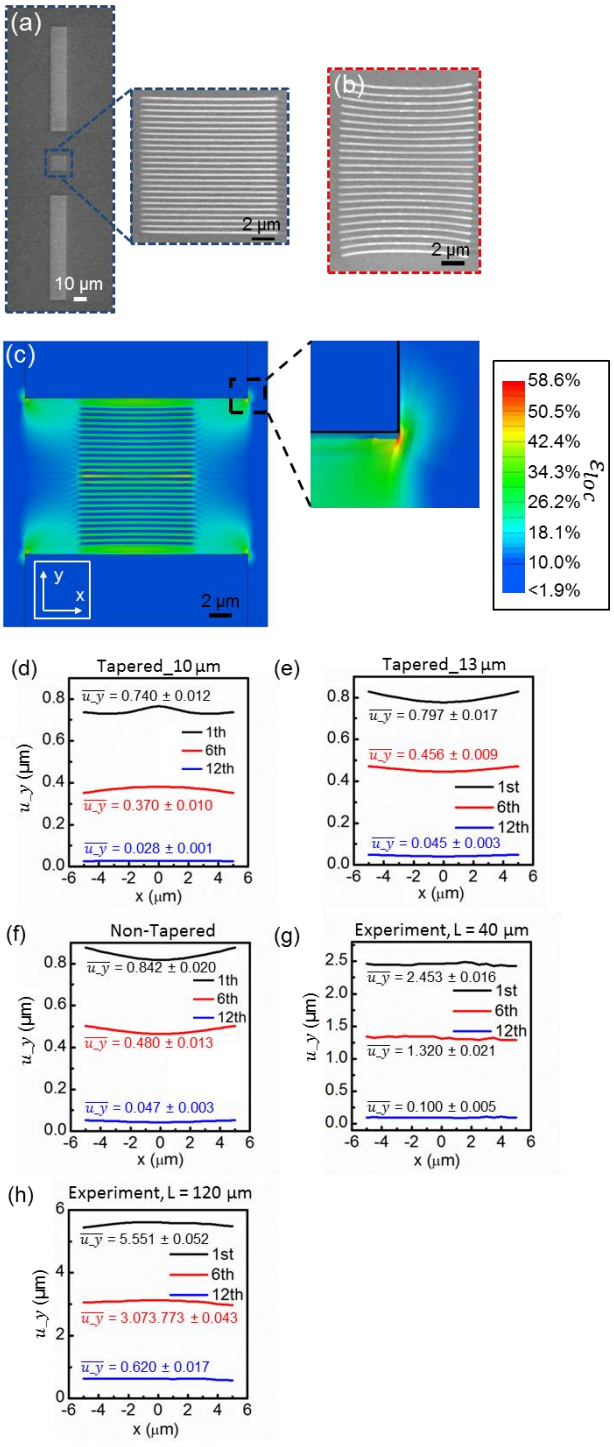

Figure S1. Non-uniform strain distribution at the corners and edges of the microrods. (a) SEM images of a pair of microrods with L = 80 μm, B = 0, W = 12 μm, T = 40 nm, and G = 50 μm. The magnified SEM image in the gap area shows a plasmonic grating with l = 12 μm, w =140

nm, and t = 40 nm on a pitch p = 470 nm. The width of the microrod is designed to be the same as the length of the Au nanolines, i.e., $\frac{W}{l} = 1$. (b) ε_{ex} = 30% is applied to the PDMS substrate. The Au nanolines at the top and the bottom of the plasmonic grating bend in the shape of an arc. (c), For ε_{ex} = 3%, finite element (FE) simulation shows the strain distribution on the surface of PDMS substrate for the non-tapered microrod (A = 20 μm, $\frac{W}{l} = 2$). The magnified image shows "hot spots" of the extremely high local strain at the corners of the microrods. The color scale represents the local strain in the y-direction on the PDMS surface (ε_{loc}). The displacement of the 1st, 6th, and 12th Au nanolines in the grating (counting from top to bottom) at ε_{ex} = 3% for the tapered microrod with 10 μm topline (A = 10 μm, d), the tapered microrod with 13 μm topline (A = 13 μm, e), and non-tapered microrod (A = 20 μm, f) based on FE modeling. u_y of the experimentally fabricated Au nanolines at ε_{ex} = 11.8% for the microrods with L = 40 μm, G = 16 μm (g) and L = 120 μm, G = 16 μm (h). The average displacement ($u\_\bar{y}$) of the Au nanolines and the standard errors are indicated in the figure.

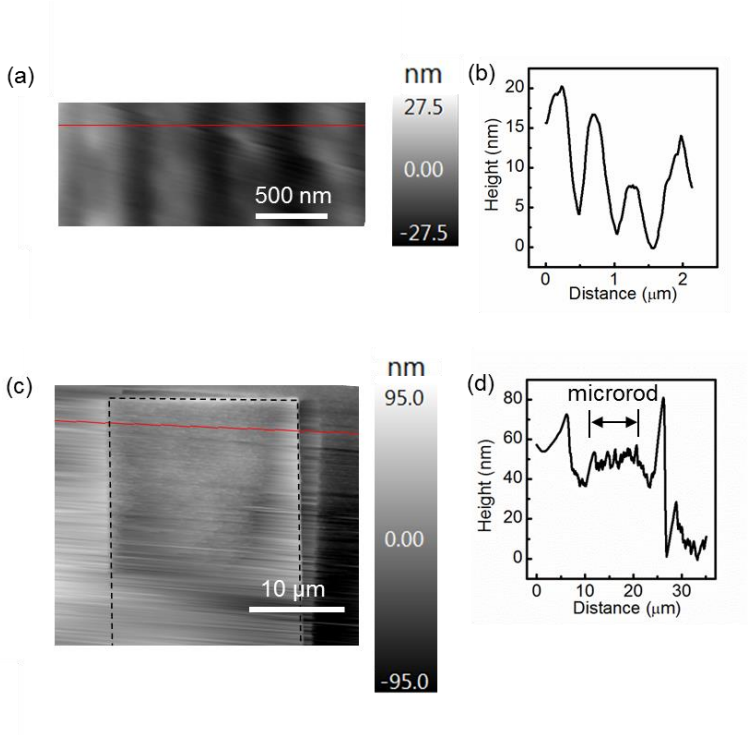

Figure S2. (a) Atomic force microscope (AFM) image of the grating and (b) the corresponding height profile along the horizontal red line. (c) AFM image of the microrod (marked by dashed lines) and (d) the corresponding height profile along the horizontal red line. The roughness of the Au layer on PDMS is approximately 3 nm according to the line cut analysis of the microrod (d).

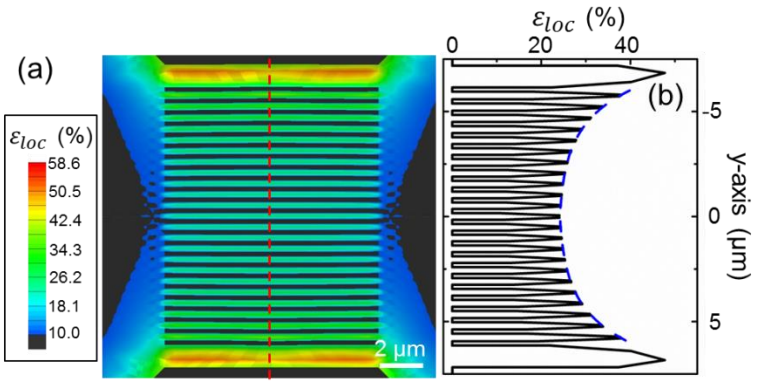

Figure S3. Magnified view of the distribution of ε_{loc} in the plasmonic grating region. (a) FE modeling of ε_{loc} on the surface of a PDMS substrate with ε_{ex} = 3%. The dimensions of the modeled metastructure are the same as those in Figure 1c,d in main text. (b) The profile of ε_{loc} along the red dashed line in (a). $\varepsilon_{spacing}$ in the plasmonic grating is fit with an exponential function, $\varepsilon_{loc} = 23.73 + 0.46 \times \exp\left(\frac{|y|}{1.69}\right)$, with an r-square above 0.999 (blue dashed line).

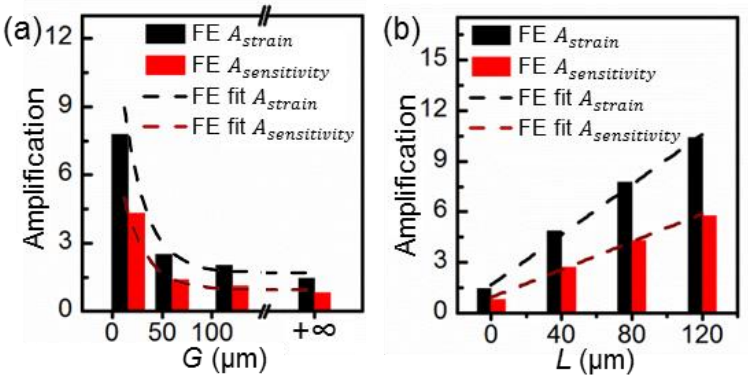

Figure S4. A_{strain} and $A_{sensitivity}$ obtained from FE models for metastructures with various G and L at ε_{ex} = 11.8%. (a) A_{strain} and $A_{sensitivity}$ as a function of G with L fixed at 80 μm. Fitting of $A_{strain} = 12.30 \times \exp\left(\frac{-G}{22.71}\right) + 1.70$ (black dashed line) and $A_{sensitivity} = 6.83 \times \exp\left(\frac{-G}{22.71}\right) + 0.94$ (red dashed line), with r-square of 0.98. (b) A_{strain} and $A_{sensitivity}$ as a function of L with G fixed at 16 μm. Fitting of $A_{strain} = 0.07 \times L + 1.67$ (black dashed line) and $A_{sensitivity} = 0.04 \times L + 0.93$ (red dashed line), with r-square of 0.995.

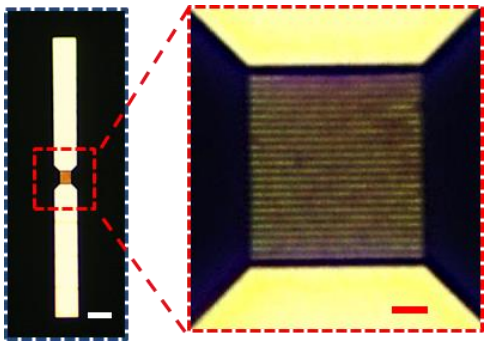

Figure S5. Metastructure released from strain. Optical microscope image of the metastructure with G = 16 μm and L = 120 μm after the PDMS is released from ε_{ex} = 11.8%. White scale bar = 20 μm and red scale bar = 2 μm.

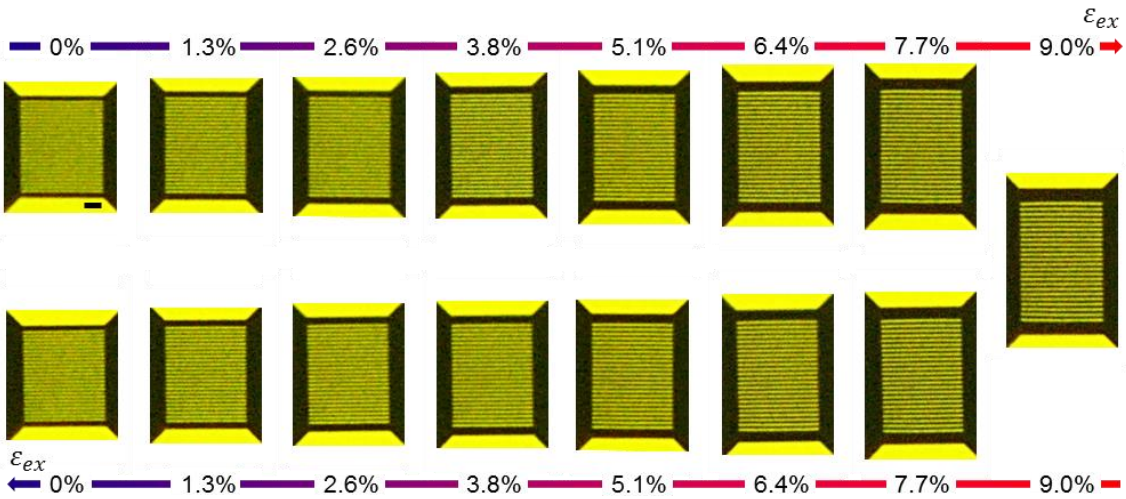

Figure S6. Mechanical responses of metastructures under continuous loading and unloading of ε_{ex}. Optical microscope images of the metastructure with G = 16 μm and L = 40 μm at various ε_{ex}. The applied ε_{ex} is denoted on top or on bottom of each figure, increasing from 0% to 9.0% and decreasing from 9.0% to 0% in steps of approximately 1.3%. Scale bar = 2 μm.

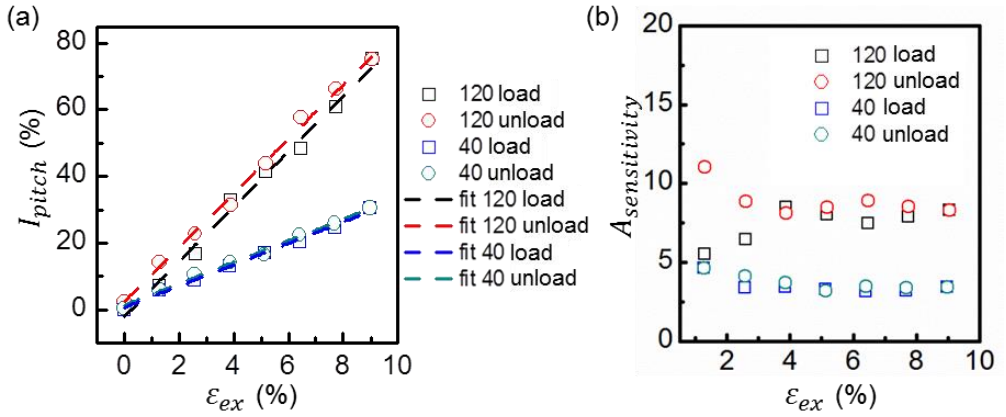

Figure S7. (a) Fitting of mechanical responses of metastructures. The linear fitting of I_{pitch} as a function of ε_{ex} (%) for the metastructures with G = 16 μm and with L = 120 μm (black, red symbols) and 40 μm (blue, green symbols). Square (circle) symbols are for loading (unloading) strain. The linear fitting results are: $I_{pitch} = 8.3 \times \varepsilon_{ex} \times 100 - 2.1$, black dashed line; $I_{pitch} = 8.2 \times \varepsilon_{ex} \times 100 + 2.3$, red dashed line; $I_{pitch} = 3.2 \times \varepsilon_{ex} \times 100 + 0.6$, blue dashed line; $I_{pitch} = 3.2 \times \varepsilon_{ex} \times 100 + 1.3$, green dashed line. The r-square for all the fittings are at or above 0.99. (b) $A_{sensitivity}$ is plotted as a function of ε_{ex} for the metastructures with G = 16 μm and with L = 120 μm (black, red symbols) and 40 μm (blue, green symbols).

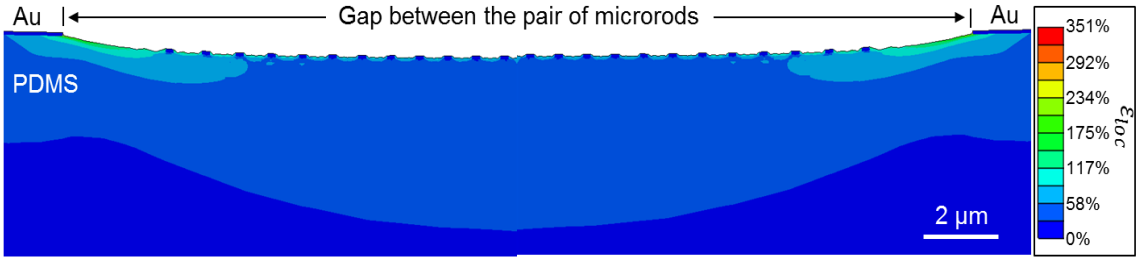

Figure S8. The cross-sectional image of the Au nanolines on PDMS substrate at ε_{ex} = 11.8% by FE modeling.

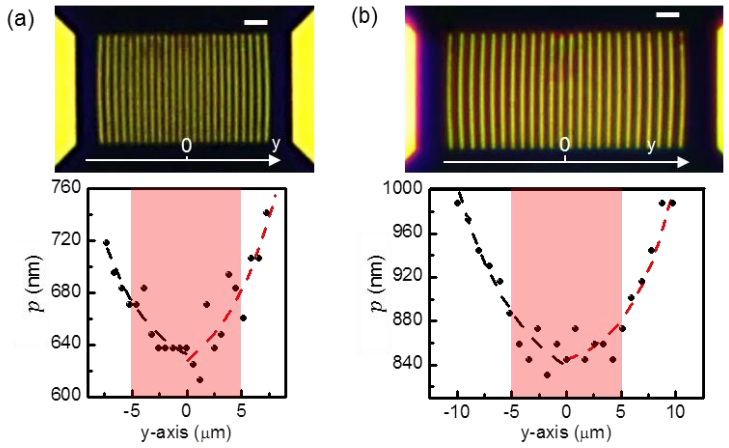

Figure S9. Optical images and quantitative analyses of the spacing between neighboring Au nanolines in the plasmonic grating. The metastructure design is G = 16 μm and L = 120 μm. The spacing between the neighboring Au nanolines in y < 0 and y > 0 regions are plotted along the y-axis and fit with the exponential function at ε_{ex} = 6.5% (a) and ε_{ex} = 11.8% (b). (a) $p = 19.7 \times \exp(-\frac{y}{4.5}) + 612.6$, r-square = 0.88 (black dashed line) and $p = 31.1 \times \exp(\frac{y}{4.9}) + 597.1$, r-square = 0.73 (red dashed line). (b) $p = 37.7 \times \exp(-\frac{y}{6.0}) + 799.5$, r-square = 0.91 (black dashed line) and $p = 13.8 \times \exp(\frac{y}{3.8}) + 830.1$, r-square = 0.90 (red dashed line). The pink region indicates the center area of the grating (10 μm × 10 μm). In the center area, the standard deviation in p' is 23 nm for ε_{ex} = 6.5% and 16 nm for ε_{ex} = 11.8%, which are comparable to the fabrication tolerance at ε_{ex} = 0%. Scale bar = 2 μm.

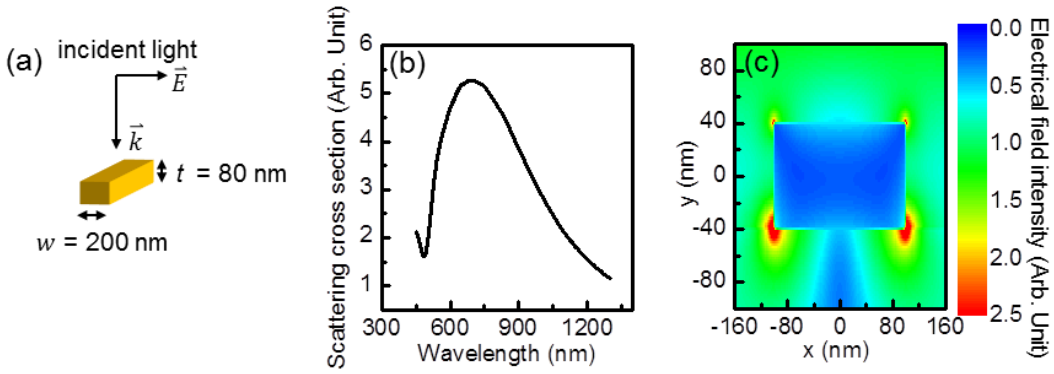

Figure S10. FDTD simulation of the optical response of an individual Au nanoline. (a) Schematic of the individual Au nanoline used in FDTD simulations. The width and the thickness of the nanoline are set to the same dimensions as those in experiments (Figure 1c,d in main text). The incident light is linearly polarized along the transverse direction of the nanoline. (b) FDTD simulation result for the scattering cross section of the individual Au nanoline. (c) Electrical field intensity map in the cross-sectional plane of an individual Au nanoline at 693 nm wavelength. The transverse section of the Au nanoline is positioned in the center of the map.

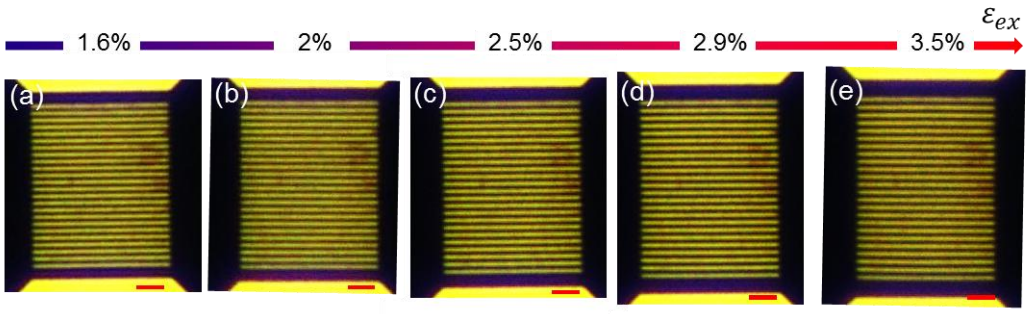

Figure S11. Metastructure under ε_{ex} variations. Optical microscope images of the metastructure with G = 16 μm and L = 120 μm when the ε_{ex} is gradually varied from 1.6% (a) to 2.0% (b), 2.5% (c), 2.9% (d), and 3.5% (e). Scale bar = 2 μm.

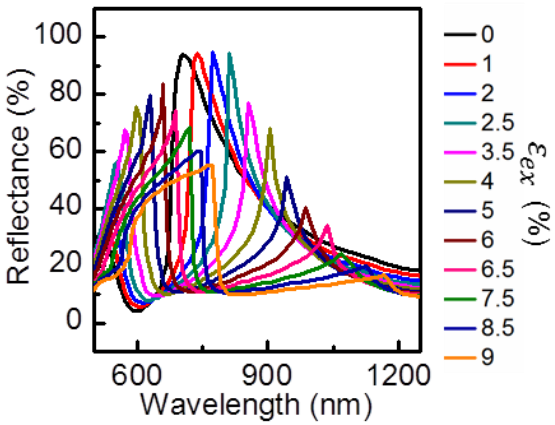

Figure S12. FDTD simulation results for the reflectance spectra of the plasmonic grating. In the simulation, the plasmonic grating has a width w = 200 nm, a thickness t = 80 nm, and a p varying from 440 nm to 770 nm in steps of 30 nm. Light is at normal incidence with y-polarization. p is directly related with ε_{ex} applied to the metastructure. p varying from 440 nm to 770 nm approximately corresponds to ε_{ex} varying from 0% to 9% based on the fitting equation in Figure S7a (black dashed line).

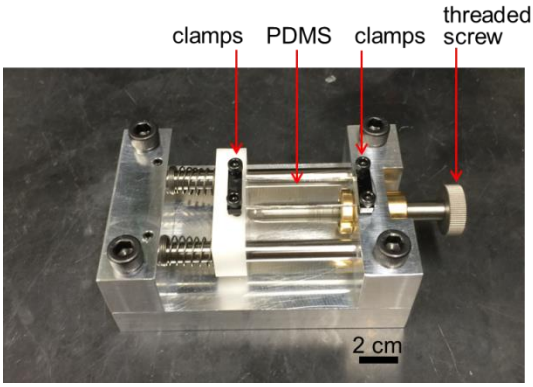

Figure S13. The custom mechanical stretcher used to apply external strain to the metastructures. The PDMS substrate is fixed by two clamps on the stage and a threaded screw is rotated to apply the external strain.

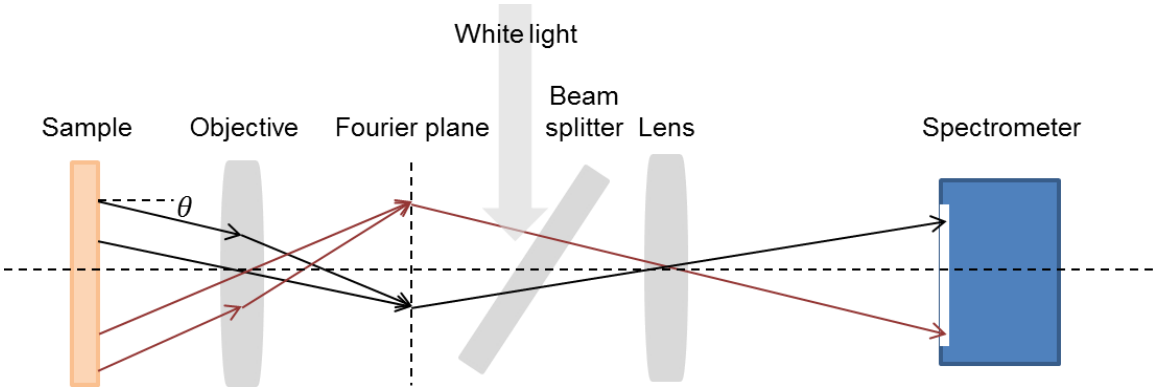

Figure S14. Schematic of the home-built angle-resolved reflectance measurement system.

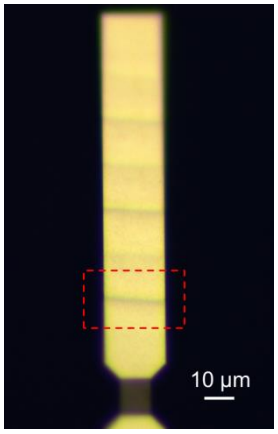

Figure S15. Buckling effect on the microrods. Microscope image of the metastructure with G = 16 μm and L = 120 μm after stretching and releasing between ε_{ex} = 9.1% and ε_{ex} = 0% cyclically for 10 times. The red dashed rectangular indicates an area of the microrod that shows buckling after cyclical stretching.

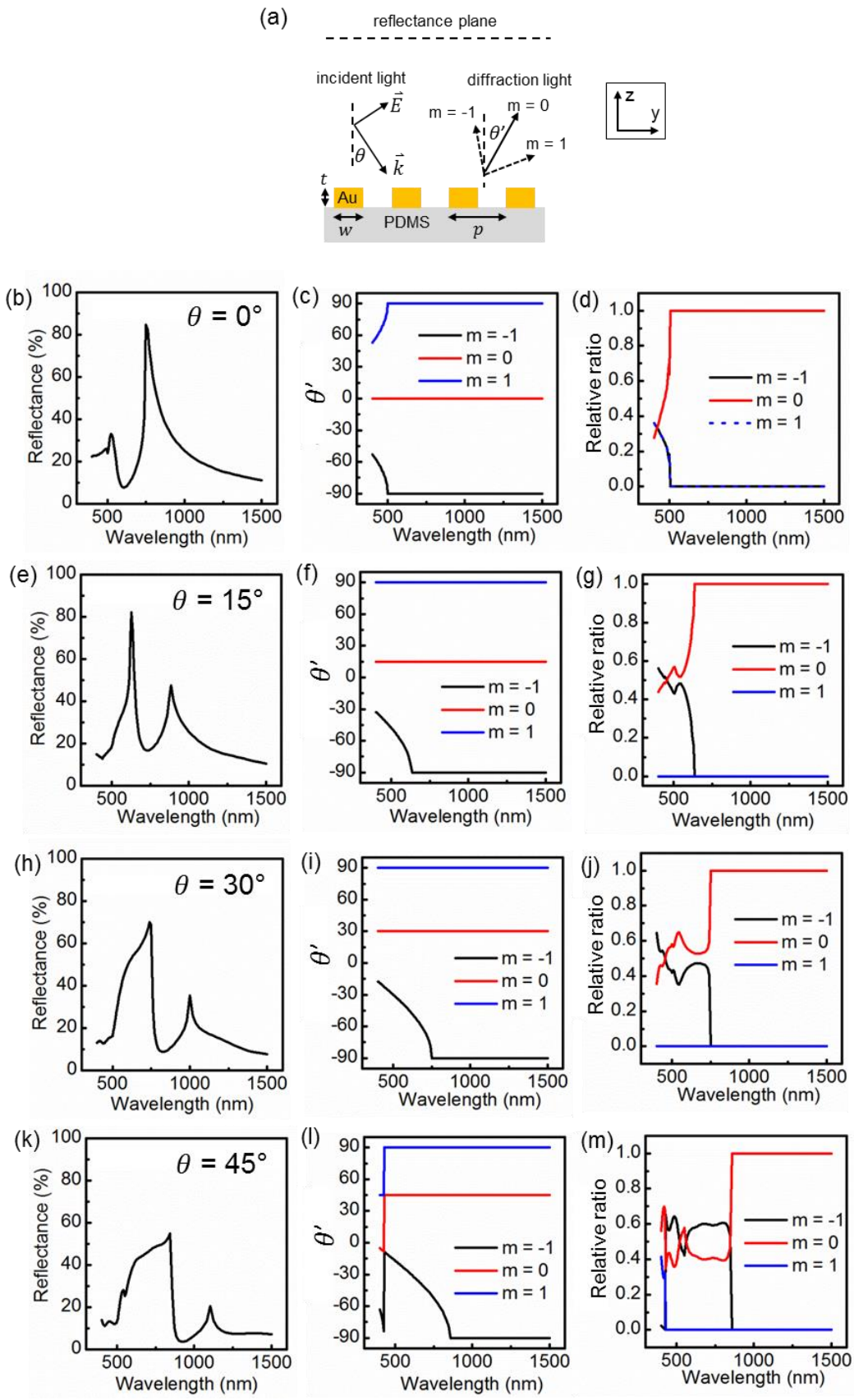
(a)
reflectance plane
incident light
diffraction light
m = -1
m = 0
m = 1
z
y
t
Au
PDMS
w
p
(b)
θ = 0°
(c)
(d)
(e)
θ = 15°
(f)
(g)
(h)
θ = 30°
(i)
(j)
(k)
θ = 45°
(l)
(m)
Reflectance (%)
θ′
Relative ratio
Wavelength (nm)

Figure S16. (a) Schematic showing the incident angle (θ), angle of different diffractive orders (θ'), and the reflectance plane for the Au plasmonic grating on the PDMS substrate used in FDTD simulations. The reflectance plane collects all the diffractive orders in the reflectance angle from -90° to 90°. For θ = 0°: (b) Reflectance of the plasmonic grating. (c) Angle of different diffractive orders. (d) The relative ratio of the intensity of the different diffractive orders in the reflectance light. (e-g), (h-j), and (k-m) are for θ = 15°, 30°, and 45°, respectively.